Predicting Hyperoxia-Induced Lung Injury from Associated Intestinal and Lung Dysbiosis in Neonatal Mice

Chung-Ming Chen (cmchen@tmu.edu.tw)
Taipei Medical University Hospital https://orcid.org/0000-0001-8762-8957
Hsiu-Chu Chou
Taipei Medical University
Yu-Chen Yang
Taipei Medical University
Emily Chia-Yu Su
Taipei Medical University

Research

Keywords: Hyperoxia, Microbiota, Mean linear intercept, Vascular endothelial growth factor, von Willebrand factor, Occludin, Zonula occludens

Posted Date: August 6th, 2020

DOI: https://doi.org/10.21203/rs.3.rs-52280/v1

Version of Record: A version of this preprint was published at Neonatology on January 1st, 2021. See the published version at https://doi.org/10.1159/000513553.

Abstract

Background: Newborns with respiratory disorders often require supplemental oxygen. Preclinical studies have demonstrated that hyperoxia disrupts the intestinal barrier, impairs intestinal function, and injures the lungs of newborn animals. The effects of neonatal hyperoxia on intestinal and lung microbiota and the role of the intestinal microbiota in the pathogenesis of hyperoxia-induced lung injury have not been investigated.

Results: In this study, we evaluated the effect of neonatal hyperoxia on intestine and lung microbiota alterations in neonatal C57BL/6N mice reared in either room air (RA) or hyperoxia (85% O_2) from postnatal days 1 to 7. On postnatal day 7, lung and intestinal microbiota were sampled from the left lung and lower gastrointestinal tract for 16S ribosomal RNA gene sequencing. Tissue from the right lung and terminal ileum were harvested for Western blot and histology analysis. Hyperoxia decreased body weight, induced intestinal injury, decreased intestinal tight junction expression, impaired lung alveolarization and angiogenesis, and increased lung cytokines in neonatal mice. Hyperoxia also altered intestinal and lung microbiota and promoted bacterial translocation from the intestine to the lung as evidenced by the presence of intestinal bacteria in the lungs of hyperoxia-exposed neonatal mice. The relative abundance of these bacterial taxa was significantly positively correlated with lung cytokines. Intestinal and lung microbiota combined with cytokines were incorporated into machine learning algorithms to develop prediction models for the classification of RA- or hyperoxia-reared mice. The experiment results demonstrated that a Bayes network achieved the best predictive performance, attaining accuracy, sensitivity, specificity, and area under the curve values of 94.4%, 88.9%, 100%, and 0.963, respectively. Selected discriminative features included lung cytokines (interleukin-1β, macrophage inflammatory protein-2, and tumor necrosis factor-α), lung microbiota (*Ruminococcaceae_UCG-010*, *CAG-56*, and *Enterobacter*), and intestinal microbiota (*Peptococcaceae_ge*, *Muribaculum*, *Enterobacter,* and *Ruminococcaceae_UCG-010*).

Conclusions: Neonatal hyperoxia exposure during the first week of life induced intestinal and lung dysbiosis and promoted bacterial translocation from the intestine to the lung. These findings suggest that changes in the composition of the intestinal microbiota contribute to hyperoxia-induced lung injury and that the combination of intestinal and lung microbiota may indicate hyperoxia-induced lung injury in neonatal mice.

Background

Newborns with respiratory distress frequently require supplementary oxygen treatment. Nevertheless, high-concentration and sustained oxygen exposure increase oxidant stress and result in lung injury. Neonatal rodents exposed to prolonged hyperoxia displayed impaired alveolarization comparable to human bronchopulmonary dysplasia [1, 2]. Bronchopulmonary dysplasia is a major cause of morbidity and mortality in preterm infants even when they are treated under the best ventilation policies such as increased use of noninvasive ventilation and early administration of a surfactant. Many infants with

bronchopulmonary dysplasia face significant respiratory morbidity, including reactive airway dysfunction and the development of obstructive lung disease during childhood [3–5]. However, no effective clinical management strategy has been proposed to prevent the development of bronchopulmonary dysplasia in preterm infants.

High concentrations of inhaled oxygen were found to increase the partial pressure of oxygen in the intestinal tissues of mice [6]. Preclinical studies have demonstrated that hyperoxia injures the distal small intestine and disrupts intestinal function in neonatal animals. These injuries are manifested as increased thickness of the ileal mucosa, an increased intestinal secretory immunoglobulin A level, an increase in serosal and submucosal vasodilation and vascularization, distortion of the villus structure, and disruption of the intestinal barrier [7–11]. Disruption of the gut barrier function induces translocation of pathogens through the epithelial layer to the lamina propria and then to the mesenteric lymph nodes, where they invade the bloodstream and disseminate to other sterile organs [12].

Lung and gut microbiota play several crucial roles in the development, regulation, and preservation of healthy states [13]. Evidence suggests that the influence of host–microbe interactions may extend beyond the local environment to peripheral tissues [14]. Hyperoxia exposure has been observed to change the bacterial composition of neonatal mice and rats' intestines [15, 16]. Numerous studies have identified the influence of the gut microbiota on lung immunity, referred to as the gut–lung axis, which is mediated mostly by inflammation involving the translocation of bacteria across the intestinal tract barrier and into blood vessels [17]. However, to date, no study has evaluated the effects of hyperoxia on lung microbiota or the role of the gut microbiome in the pathogenesis of hyperoxia-induced lung injury. We found that hyperoxia increased intestinal permeability and the translocation of bacteria from the gastrointestinal tract to the liver and spleen in newborn rats [18]. We hypothesized that neonatal hyperoxia alters intestinal and lung microbiota and that hyperoxia-induced lung injury is driven by the gut microbiota through gut–lung communication. The aims of this study were to investigate the effects of hyperoxia on the lung and intestinal microbiota and the communication between intestinal and lung microbiota and to develop a predictive model for the identification of hyperoxia-induced lung injury from intestinal and lung microbiota based on machine learning algorithms in neonatal mice.

Results

Survival rate and body weight

Four pregnant C57BL/6N mice gave birth to a total of 22 pups; 9 and 13 pups were distributed to the RA and hyperoxia groups, respectively. All 9 mice reared in RA survived. However, two mice reared in O_2-enriched air died on postnatal day 5 (Fig. 1a). Mice reared in hyperoxia exhibited significantly lower body weights on postnatal day 7 than did those reared in RA (Fig. 1b).

Hyperoxia induced intestinal injury and decreased intestinal tight junction expression

Representative sections of the intestines of mice exposed to postnatal RA or hyperoxia were stained with hematoxylin and eosin, and these are illustrated in Fig. 2a. The mice reared in RA exhibited a normal intestinal mucosal framework and well-defined intercellular space at the basal portion of the enterocytes. The mice reared in hyperoxia had malalignment and distended basolateral intercellular spaces in the epithelium and exhibited a significantly higher intestinal injury score than did RA-reared mice. The results of immunohistochemistry and Western blotting for occludin and zonula occludens (ZO)-1 are presented in Fig. 2b, c. Both occludin and ZO-1 were observed on the side adjacent to the cell membranes of the enterocytes. The hyperoxia-reared mice exhibited disrupted occludin and ZO-1 immunohistochemistry between adjacent enterocytes. The hyperoxia-reared mice exhibited significantly lower occludin and ZO-1 protein levels than did RA-reared mice.

Hyperoxia impaired alveolarization and angiogenesis in neonatal mice

Representative lung sections from mice exposed to postnatal RA or Hyperoxia that were stained with hematoxylin and eosin are depicted in Fig. 3a. Those from the mice reared in hyperoxia exhibited large thin-walled air spaces and significantly higher mean linear intercepts (MLIs) than did those from mice reared in RA (Fig. 3a). The representative immunohistochemistry of vascular endothelial growth factor (VEGF) and von Willebrand factor (vWF) are presented in Fig. 3b, c. The mice reared in hyperoxia exhibited significantly decreased VEGF and vWF immunoreactivity. Western blot analysis and semiquantitative analysis revealed that the mice reared in hyperoxia exhibited significantly decreased VEGF protein expression and vascular density than did those reared in RA.

Hyperoxia increased lung cytokines levels

The mice reared in hyperoxia exhibited significantly higher interleukin-1β (IL-1β), tumor necrosis factor-α (TNF-α), and macrophage inflammatory protein-2 (MIP-2) levels than did those reared in RA (Fig. 3d).

Hyperoxia altered intestinal and lung microbiota

The 16S rDNA were purified from the stool of the lower intestines and lungs of mice, and sequencing was performed with the Illumina MiSeq System through analysis of the V3-V4 region. Hyperoxia treatment was revealed to influence the community richness and reduce alpha diversity in the intestine microbiota (Fig. 4a). Nonmetric multidimensional scaling (NMDS) based on unweighted UniFrac distances also revealed that hyperoxia-reared mice displayed an intestine microbiota profile different from that of the RA-reared mice ($P = 0.01399$; Fig. 4b). In hyperoxia-reared mice, *Firmictes*, *Epsilonbacteraeota*, and *Actinobacteria* were significantly decreased in microbial composition at the phylum level compared with in RA-reared mice (Fig. 4c, d). Also, significant microbial changes were found at the genus level including for *Finegoldia*, *Prevotella*, *Enterobacter*, *Peptoniphilus*, *Prevotella_6*, *Anaerococcus*, *Sneathia*, *Megasphaera*, *Acidaminococeus*, *Epsllonbacteraeota*, *Campylobacter*, *Mitsuokella*, *Gardnerella*, *Porphyromonas*, *Corynebacterium*, *Muribaculaceae_ge*, *Alphaproteobacteria*, *Prevotella_7*, *Sphingomonas*, *Neisseria*, *Haemophilus*, *Pasteurellales*, *Murdochiella*, *Veillonella*, *Brevundimonas*, *Atopobium*, *Gemella*, *DNF00809*, *Mobiluncus*, *Negativicoccus*, *Novosphingobium*, *Lawsonella*, *Citrobacter*,

Enterorhabdus, *Methylobacterium*, *Brochybacterium*, *Muribaculum*, *Fusobacteriaceae_ge*, *Ruminiclostridium_6*, *GCA_900066575*, *Enterococcaceae_ge*, *Leptotrichiaceae_ge*, *Comamonas, Proteus*, *Erysipelotrichaceae_UCG_003*, and *Escherichia_Shigella* (Fig. 4c, d).

Evaluation of the lung microbiota revealed that hyperoxia-reared mice exhibited significantly increased alpha diversity compared with RA-reared mice (Fig. 5a). NMDS analysis also showed that hyperoxia-reared mice displayed different lung microbiota profiles compared with RA-reared mice ($P = 0.01898$; Fig. 5b). Significant changes occurred at the genus level, including to *Corynebacteriaceae_ge*, *Corynebacterium*, *Lawsonella*, *Prevotella_7*, *Flavobacterium*, *Aneaerococcus*, *Coproccus_2*, *Lachnospira*, *Peptococcus*, *Ruminococcaceae_UCG_002*, *Ruminococcaceae_UCG_010*, *Ruminococcus_1*, *Holdemanella*, *Comamonas*, *Massilia*, and *Enterobacter* (Fig. 5c, d).

Hyperoxia promoted bacterial translocation from the intestine to the lung

In this study, to explore the relevance of the gut–lung axis, we analyzed the types of strains at the genus level and detected *CAG-56*, *Clostridia_Family_XIII_ge*, *Coriobacteriales_Incertae_Sedis_ge*, *Enterobacter*, *Howardella*, *Muribaculum*, *Peptococcaceae_ge*, *Ruminococcaceae_UCG-010*, *Sellimonas*, and *Weissella* in the intestines of both types of mice but only in the lungs of hyperoxia-reared mice (Table 1). In addition, Spearman correlation coefficients revealed a significant positive correlation between lung microbiota translocated from the intestine and pulmonary inflammatory cytokines (Table 2). IL-1β levels in the lungs were significantly positively correlated with MIP-2, *Muribaculum*, *Peptococcaceae_ge*, and *Sellimonas* ($P < 0.05$). TNF-α levels in the lungs were significantly positively correlated with *CAG-56* ($P < 0.01$), *Ruminococcaceae_UCG-010* ($P < 0.01$), and *Clostridia_Family_XIII_ge* ($P < 0.05$). Notably, the relative abundances of these bacterial taxa were also significantly positively correlated, including those of *CAG-56*, *Clostridia_Family_XIII_ge*, *Coriobacteriales_Incertae_Sedis_ge*, *Ruminococcaceae_UCG-010*, *Sellimonas*, and *Weissella* (Table 2).

Use of machine learning algorithms for accurately classifying RA- and hyperoxia-treated groups based on lung cytokines and microbiota

The lung and intestinal microbiota (10 from lungs and 10 from intestines) analyzed in Table 1 and three lung cytokines (IL-1β, TNF-α, and MIP-2) were incorporated to develop prediction models. Weka software was used to distinguish between RA- and hyperoxia-reared mice. The experiment results in Table 3 demonstrate that the use of the microbiota combined with cytokines yielded accurate predictive results evaluated through leave-one-out cross-validation (LOOCV). Three algorithms, including a Bayes network, decision tree, and *k*-nearest neighbor, yielded satisfactory predictive performance. The Bayes network performed better than did the other algorithms for accuracy, sensitivity, specificity, and area under the curve, attaining values of 94.4%, 88.9%, 100%, and 0.963, respectively. Moreover, to further identify the important variables for the classification of RA- and hyperoxia-reared mice, the random forest algorithm was incorporated to select discriminative features, as shown in Fig. 6a. The important features selected included lung cytokines (IL-1β, MIP-2, and TNF-α), lung microbiota (e.g., *Ruminococcaceae_UCG-010*,

CAG-56, and *Enterobacter*), and intestinal microbiota (e.g., *Peptococcaceae_ge*, *Muribaculum*, *Enterobacter*, and *Ruminococcaceae_UCG-010*).

Discussion

Our *in vivo* model demonstrated that hyperoxia exposure during the first 7 days after birth induced intestinal and lung injury in neonatal mice, as evidenced by increased intestinal injury scores, decreased intestinal barrier integrity, increased lung inflammation, and reduced alveolarization and angiogenesis. Hyperoxia-induced intestinal and lung injuries were associated with intestinal and lung dysbiosis. Several pathogenic bacteria present in the gastrointestinal tract were found in the lungs of hyperoxia-exposed newborn mice, and this suggested a significant positive correlation between the translocation of lung microbiota from the intestines and the presence of pulmonary cytokines. These findings suggest that translocation of intestinal bacteria to the lungs contributes to hyperoxia-induced lung injury and that depletion of the intestinal microbiome might reduce hyperoxia-induced lung injury. These results support the concept that the lung microbiome represents a novel therapeutic target for the prevention and treatment of lung injury [19].

In this study, we selected C57BL/6N mice as an animal model for hyperoxia-induced lung injury because the C57BL/6N mouse strain is more sensitive to hyperoxia-induced perturbations in alveolar development than are other strains [20]. On postnatal day 7, we observed that mice reared in hyperoxia exhibited significantly lower body weights than did those reared in RA. These results are compatible with those of another study that found hyperoxia to reduce body weight in C57BL/6N mice [21]. In our other studies, we have demonstrated that hyperoxia exposure during the first 7 days of life induces lung injury, reduces alveolarization and angiogenesis, injures the distal small intestine, disrupts the intestinal barrier, and impairs intestinal function in newborn Sprague Dawley rats [22, 23]. In this study, we used C57BL/6N newborn mice and found similar injury patterns in the intestines and lungs. These results suggest that the C57BL/6N mouse model is suitable for the investigation of hyperoxia effects on the intestines and lungs of newborn animals.

Alterations in the intestinal microbiota composition contribute to the pathogenesis of many pulmonary diseases including chronic obstructive pulmonary disease, asthma, and cystic fibrosis [24–26]. The role of intestinal microbiota in hyperoxia-induced lung injury remains unknown. In this study, we demonstrated that hyperoxia-induced intestinal and lung injury and altered intestinal and lung microbiota in neonatal mice. The lung microbiota was enriched with intestinal bacteria, and intestinal abundance was significantly positively correlated with lung cytokines. These results indicate that the intestinal microbiota contributes to the pathophysiology of hyperoxia-induced lung injury in neonatal mice. These findings are compatible with the finding of Dolma et al., who found that, in neonatal mice, the lung structure and mechanics are protected and inflammation is decreased for germ-free specimens [27].

In this study, we found that the lung microbiome was primarily dominated by the phyla *Bacteroidetes*, *Firmicutes*, *Proteobacteria*, *and Actinobacteria* on postnatal day 7, which is consistent with the findings of

Singh et al. [28]. We also observed that several gut-associated bacteria in the lungs of hyperoxia-reared mice and their relative abundance were significantly positively correlated with lung inflammation. Bacterial translocation is defined as the passage of viable microorganisms from the gastrointestinal tract through the epithelial barrier to the mesenteric lymph nodes and other extraintestinal organs and sites [29]. Neonatal hyperoxia-induced intestinal injury fulfills two of the three primary mechanisms promoting bacterial translocation: (a) disruption of the ecologic gastrointestinal equilibrium, leading to intestinal bacterial overgrowth, (b) increased permeability of the intestinal mucosal barrier, and (c) deficiencies in host immune defenses [30]. These results suggest that translocation of intestinal bacteria to the lungs contributes to hyperoxia-induced lung injury in neonatal mice.

Furthermore, to investigate the effects of biomedical features on hyperoxia, partial dependence plots were incorporated to evaluate the marginal effects of variables on class probability for classification. These provide insights into the influences of variables in machine learning algorithms and show the relative propensities in logit distributions of the class probabilities. The *x*-axis of each partial dependence plot shows the independent variable, and the *y*-axis depicts the changes in fraction vote for the probability of hyperoxia-reared group in each variable. Positive *y*-axis values indicate that the values of independent variables are more likely to belong to the positive class (here, we set the positive class as the hyperoxia-reared group). By contrast, negative values are less likely to belong to the positive class, and zero indicates the absence of an average influence on class probability. Figure 6b–e illustrates partial dependence plots depicting the effects of important variables on the hyperoxia-reared group. As suggested in Fig. 6b, when the value for the most influential variable, IL-1β, is more than 331, a high propensity exists for the hyperoxia-reared group. In addition, Fig. 6c demonstrates that when MIP-2 is higher than 1011, the probability that the specimen belongs to the hyperoxia-reared group is higher. In summary, results from the proposed computational approaches correspond well with medical insights. Therefore, we believe that our predictive models can be incorporated into clinical practice and may provide interpretable biomedical features for future research.

One limitation of this study is that we did not evaluate intestinal permeability. We have shown that similar levels of hyperoxia (85% O_2) exposure from postnatal days 1 to 7 reduced intestinal tight junction expression and increased intestinal permeability and bacterial translocation in newborn Sprague Dawley rats [18, 23].

Conclusions

This study demonstrated that hyperoxia induced intestinal and lung injury and dysbiosis and that the lung microbiota was enriched with gut-associated bacteria in neonatal mice. These findings suggest that the translocation of intestinal bacteria to the lungs contributes to hyperoxia-induced lung injury in neonatal mice. Currently, no effective therapy is available to prevent hyperoxia-induced lung injury. These findings suggest potential for manipulation of the gut microbiota in the prevention and treatment of hyperoxia-induced lung injury. However, further investigation is required to clarify how intestinal bacteria translocation to the lung occurs after hyperoxia exposure.

Methods

Experimental groups

We conducted experiments in accordance with the approved guidelines and regulations of the Institutional Animal Care and Use Committee of Taipei Medical University. Time-dated pregnant C57BL/6N mice were purchased from Bio-LASCO Taiwan Co., Ltd., and they were housed in individual cages with free access to laboratory food and water. A 12-h:12-h light–dark cycle was maintained. The mice were allowed to deliver vaginally at term. Within 12 h of birth, the litters were pooled and randomly redistributed among the newly delivered mothers, and the pups were then randomly assigned to be reared in room air (RA) or O_2-enriched air. The pups in the hyperoxia (O_2, normobaric) group were reared in an atmosphere containing 85% O_2 during postnatal days 1 to 7. The pups in the RA group were reared in RA during postnatal days 1 to 7. To avoid O_2 toxicity in the nursing mothers, they were rotated between the O_2 treatment litter and the RA control litter every 24 h. An O_2-rich (85%) atmosphere was maintained in a transparent 40 × 50 × 60 cm^3 plexiglass chamber, which continuously received O_2 at 4 L/min. The levels of O_2 were monitored using a ProOx P110 monitor (NexBiOxy, Hsinchu, Taiwan). Survival rates were recorded daily. On postnatal day 7, mouse pups were euthanized in a chamber with isoflurane (Halocarbon Laboratories, River Edge, NJ, USA), lung and intestinal microbiota were sampled from the left lung and lower gastrointestinal tract, and right lung and terminal ileum were harvested.

Lung and intestinal histology

To standardize analysis, sections were obtained from the right middle lobe of the right lung. The lung tissue and ileum were immersed in 4% paraformaldehyde with 0.1 M phosphate buffer (pH 7.4) at 4°C for 24 h. The tissues were then dehydrated in alcohol, cleaned in xylene, and embedded in paraffin. Five-micrometer sections were stained with hematoxylin and eosin, examined using light microscopy, and assessed for lung and intestinal morphometry. MLI, an indicator of mean alveolar diameter, was assessed in 10 nonoverlapping fields [31]. Vascular density was determined with the vWF immunohistochemistry reaction. Microvessel density was determined by counting the vessels with positive vWF staining in an unbiased manner and in a minimum of four random lung fields at ×400 magnification [32]. The intestinal mucosal injury was scored using a scale from 0 to 5 with 0 = *normal mucosal villi*, 1 = *subepithelial space at the villus tip and frequent capillary congestion*, 2 = *extension of the subepithelial space with moderate lifting of the epithelial layer from the lamina propria*, 3 = *massive epithelial lifting down the sides of villi with occasionally denuded villi tips*, 4 = *denuded villi with dilation of the lamina propria and capillaries*, and 5 = *disintegration of the lamina propria, hemorrhage, and ulceration* [33].

Immunohistochemistry of intestinal ZO-1 and occludin

After routine deparaffinization and rehydration, heat-induced epitope retrieval was performed through the immersion of slides in 0.01 M sodium citrate buffer (pH 6.0). To block endogenous peroxidase activity

and nonspecific antibody binding, the sections were first preincubated in 0.1 M phosphate buffered saline (PBS) containing 10% normal goat serum and 0.3% H_2O_2 for 1 h at room temperature before incubation with rabbit polycolonal anti-ZO-1 antibodies (1:50; Santa Cruz Biotechnology, Inc., Dallas, TX, USA) and mouse monocolonal antioccludin (1:50 dilution; Santa Cruz Biotechnology) as primary antibodies for 20 h at 4°C. The sections were then treated for 1 h at 37°C with biotinylated goat antirabbit immunoglobulin G (IgG; 1:200, Vector Laboratories, Burlingame, California, USA) for anti-ZO-1 antibodies and with biotinylated goat antimouse IgG (1:200; Jackson ImmunoResearch Laboratories, West Grove, Pennsylvania, USA) for antioccludin antibodies. Sections were subsequently reacted with reagents from an avidin–biotin complex kit (Vector Laboratories), and the brown reaction products were visualized following the use of a diaminobenzidine substrate kit (Vector Laboratories) per the manufacturer's recommendations.

Immunohistochemistry of lung VEGF and vWF

Immunohistochemical staining was performed on 5-μm paraffin sections by using immunoperoxidase visualization. After routine deparaffinization, heat-induced epitope retrieval was performed through immersion of the slides in 0.01 M sodium citrate buffer (pH 6.0). To block the endogenous peroxidase activity and nonspecific binding of antibodies, the sections were preincubated for 1 h at room temperature in 0.1 M PBS containing 10% normal goat serum and 0.3% H_2O_2. The sections were then incubated for 20 h at 4°C with rabbit polyclonal anti-vWF antibody (1:100; Abcam, Cambridge, Massachusetts, USA) or rabbit polyclonal anti-VEGF antibody (1:50; Santa Cruz Biotechnology) as primary antibodies. The sections were then treated for 1 h at 37°C with biotinylated goat antimouse or antirabbit IgG (1:200, Jackson ImmunoResesarch Laboratories Inc.). Following the reaction produced using reagents from an avidin–biotin complex kit (Vector Laboratories, Inc.), the reaction products were visualized using a diaminobenzidine substrate kit (Vector Laboratories, Inc.) according to the recommendations of the manufacturer.

Lung cytokines

IL-1β, TNF-α, and MIP-2 levels were determined using the Bio-Plex multiplex assay system (Bio-Rad, Hercules, CA, USA) and Procarta immunoassay kit (Affymetrix) according to the manufacturers' protocols.

Western blot analysis of intestinal occludin and ZO-1

Intestinal tissues were homogenized in ice-cold buffer containing 50 mmol/L Tris·HCl (pH 7.5), 1 mmol/L ethylene glycol tetraacetic acid, 1 mmol/L ethylenediaminetetraacetic acid, and a protease inhibitor cocktail (cOmplete Mini tablets; Roche, Mannheim, Germany). Proteins (30 μg) were resolved on 12% sodium dodecyl sulfate–polyacrylamide gel electrophoresis subject to reducing conditions and electroblotted to a polyvinylidene difluoride membrane (Immobilon-P, Millipore, Millipore Merck Corporation, MA, USA). After the membranes were blocked with 5% nonfat dry milk, they were incubated with antioccludin (Santa Cruz Biotechnology, Inc., CA, USA), anti-ZO-1 (750; Santa Cruz Biotechnologies,

Inc.), or anti-β-actin (1:1000; Santa Cruz Biotechnologies, Inc.). Protein bands were detected using the BioSpectrum AC System (UVP, Upland, CA, USA).

Western blot analysis of lung VEGF

Lung tissues were homogenized in ice-cold buffer, sonicated, and centrifuged to remove cellular debris. Thirty micrograms of proteins were resolved and electroblotted to a polyvinylidene difluoride membrane (Immobilon^{P}, Millipore, Bedford, MA, USA). The membranes were incubated with antibodies against VEGF (Santa Cruz Biotechnology) and anti-β-actin (Sigma-Aldrich, St. Louis, MO, USA) and subsequently with horseradish peroxidase–conjugated goat antimouse IgG (Pierce Biotechnology, Rockford, IL, USA) after blocking with 5% nonfat dry milk. We used SuperSignal substrate (Pierce Biotechnology) to detect protein bands. Densitometric analysis was performed using AIDA software to measure the intensity of VEGF and β-actin bands.

16S rRNA gene sequencing

The stools were purified using the QIAamp Fast DNA Stool Mini Kit (QIAGEN, Germany). The library preparation followed the protocol of 16S Ribosomal RNA Gene Amplicons for the Illumina MiSeq System. Sequence reads were deposited in the European Nucleotide Archive under accession number PRJEB28574. The universal primers (341F and 805R) that were used to amplify the V3-V4 region of the bacterial 16S rRNA genes were first removed from the demultiplexed paired reads by using cutadapt (v 1.12; DOI:10.14806/ej.17.1.200). The filtered reads were processed in the R environment (v 3.3.3) by using R package DADA2 (v 1.3.5) [34] according to the workflow described in Callahan et al. (2016) [35] without performing a rarefication procedure. Briefly, the forward and reversed reads were filtered and trimmed based on the read quality score and read length. Dereplication was then performed to merge identical reads, and reads were subjected to the Divisive Amplicon Denoising Algorithm 2 (DADA2), which alternates between error rate estimation and sample composition inference until convergence is obtained on a jointly consistent solution. Finally, the paired reads that required a minimum 20-bp overlap were merged, and chimeras were subsequently removed. At this point, we obtained a list of V3-V4 sequence variants (SVs) in our samples that were inferred by DADA2 as well as the SV frequency in each sample. Taxonomy assignment was performed using the SILVA database (v128) [36] as the reference, with a minimum bootstrap confidence of 80. Multiple sequence alignment of the SVs was performed with DECIPHER (v 2.2.0), and a phylogenetic tree was constructed from the alignment by using phangorn (v 2.2.0) [37]. The count table, taxonomy assignment results, and phylogenetic tree were consolidated into a phyloseq object, and community analyses were performed using phyloseq (v 1.19.1) [38]. The alpha diversity indices were calculated using the estimate richness function from the phyloseq package. Statistical comparison between treatment and control was performed with the exact Wilcoxon–Mann–Whitney test (at $\alpha = 0.05$). We analyzed sample relatedness through NMDS analysis of microbial community composition; analysis was done with the ‘mantel’ function and the Bray–Curtis dissimilarity matrix calculated using the “vegdist” function in the vegan package. Microbiota enrichment analysis between groups was conducted using the linear discriminant analysis (LDA) effect size method with

alpha set at 0.05 (Kruskal–Wallis and Wilcoxon tests) and logarithmic LDA scores of 2 or more [39]. Cladograms were employed for visualization by using GraPhlAn [40].

Predictive modeling to classify RA- and O_2-treated groups using intestinal and lung microbiota

Machine learning algorithms have been shown to be effective for comparing microbiota [41] and predicting diseases [42]. To further depict the discriminative power of lung and intestinal microbiota, the genus-level relative abundances of microbiota and lung cytokines were further incorporated as input features for distinguishing between RA- and hyperoxia-reared mice. Three machine algorithms, namely a decision tree, *k*-nearest neighbor, and Bayes network, were applied to predict the classes of the mice based on lung cytokines and microbiota. Due to the small sample size, LOOCV was incorporated to evaluate the predictive performance. One mouse was selected as the test set, and the remaining mice were used as the training set to create a machine learning model to predict the test sets to which mice belonged. This process was repeated for all mice in the data set. Subsequently, several evaluation measures including accuracy, sensitivity, specificity, and area under the receiver operating characteristic curve were used to evaluate predictive performance. We anticipate that microbiota data collected from the intestines and lungs can achieve satisfactory predictive performance and identify discriminative biomedical features for clinical practice.

Statistical analysis

All data were presented as mean ± standard deviation (SD). Student's *t* test was used to compare the RA- and O_2-treated groups. The survival rate was evaluated using the Kaplan–Meier method, and a log-rank test was utilized for comparison between groups. A P value < 0.05 was considered statistically significant.

Abbreviations

AUC: area under the curve; IL-1β: interleukin-1β; LOOCV: leave-one-out cross-validation; MIP-2: macrophage inflammatory protein-2; MLI: mean linear intercept; NMDS: nonmetric multidimensional scaling; RA: room air; SVs: sequence variants; TNF-α: tumor necrosis factor-α; VEGF: vascular endothelial growth factor; vWF: von Willebrand factor; ZO: zonula occludens.

Declarations

Acknowledgments

Not applicable.

Authors' contributions

CMC conceptualized and designed the experiments. CMC, HCC, YCY, and CYS performed experiments and analyzed experimental results. CMC, HCC, YCY, and CYS drafted the manuscript. All authors read and

approved the final manuscript.

Funding

This study was supported by a grant from the Ministry of Science and Technology in Taiwan (MOST 109-2314-B-038-073).

Consent to publication

Not applicable.

Competing interests

The authors declare that they have no competing interests.

References

1. Manji JS, O'Kelly CJ, Leung WI, Olson DM. Timing of hyperoxic exposure during alveolarization influences damage mediated by leukotrienes. Am J Physiol Lung Cell Mol Physiol. 2001;281:L799–806.
2. Chen CM, Wang LF, Chou HC, Lan YD, Lai YP. Up-regulation of connective tissue growth factor in hyperoxia-induced lung fibrosis. Pediatr Res. 2007;62:128–33.
3. Gien J, Kinsella JP. Pathogenesis and treatment of bronchopulmonary dysplasia. Curr Opin Pediatr. 2011;23:305–13.
4. Jacob SV, Coates AL, Lands LC, MacNeish CF, Riley SP, Hornby L, et al. Long-term pulmonary sequelae of severe bronchopulmonary dysplasia. J Pediatr. 1998;133:193–200.
5. Northway WH Jr, Moss RB, Carlisle KB, Parker BR, Popp RL, Pitlick PT, et al. Late pulmonary sequelae of bronchopulmonary dysplasia. N Engl J Med. 1990;323:1793–9..
6. Albenberg L, Esipova TV, Judge CP, Bittinger K, Chen J, Laughlin A, et al. Correlation between intraluminal oxygen gradient and radial partitioning of intestinal microbiota. Gastroenterology. 2014;147:1055–63.e8.
7. Giannone PJ, Bauer JA, Schanbacher BL, Reber KM. Effects of hyperoxia on postnatal intestinal development. Biotech Histochem. 2007;82:17–22.
8. Li N, Ma L, Liu X, Shaw L, Li Calzi S, Grant MB, et al. Arginyl-glutamine dipeptide or docosahexaenoic acid attenuates hyperoxia-induced small intestinal injury in neonatal mice. J Pediatr Gastroenterol Nutr. 2012;54:499–504.
9. Liu DY, Li JJ. Effect of hyperoxia on the intestinal IgA secretory component in neonatal rats and on intestinal epithelial cells in vitro. Braz J Med Biol Res. 2010;43:1034–41.
10. Torbati D, Tan GH, Smith S, Frazier KS, Gelvez J, Fakioglu H, et al. Multiple-organ effect of normobaric hyperoxia in neonatal rats. J Crit Care. 2006;21:85–93.

11. 11Chen CM, Chou HC. Hyperoxia disrupts the intestinal barrier in newborn rats. Exp Mol Pathol. 2016;101:44–9.
12. Assimakopoulos SF, Triantos C, Maroulis I, Gogos C. The role of the gut barrier function in health and disease. Gastroenterol Res. 2018;11:261–3.
13. Tamburini S, Shen N, Wu HC, Clemente JC. The microbiome in early life: implications for health outcomes. Nat Med. 2016;22:713–22.
14. Amon P, Sanderson I. What is the microbiome? Arch Dis Child Educ Pract Ed. 2017;102:257–60.
15. Althouse MH, Stewart C, Jiang W, Moorthy B, Lingappan K. Impact of early life antibiotic exposure and neonatal hyperoxia on the murine microbiome and lung injury. Sci Rep. 2019;9:14992.
16. Wedgwood S, Warford C, Agvatisiri SR, Thai PN, Chiamvimonvat N, Kalanetra KM, et al. The developing gut-lung axis: postnatal growth restriction, intestinal dysbiosis, and pulmonary hypertension in a rodent model. Pediatr Res. 2020;87:472–9.
17. Schuijt TJ, Lankelma JM, Scicluna BP, de Sousa e Melo F, Roelofs JJ, de Boer JD, et al. The gut microbiota plays a protective role in the host defence against pneumococcal pneumonia. Gut. 2016;65:575–83.
18. Chou HC, Chen CM. Neonatal hyperoxia disrupts the intestinal barrier and impairs intestinal function in rats. Exp Mol Pathol. 2017;102:415–21.
19. Dickson RP, Schultz MJ, van der Poll T, Schouten LR, Falkowski NR, Luth JE, et al. Lung microbiota predict clinical outcomes in critically ill patients. Am J Respir Crit Care Med. 2020;201:555–63. .
20. Tiono J, Surate Solaligue DE, Mižíková I, Nardiello C, Vadász I, Böttcher-Friebertshäuser E, et al. Mouse genetic background impacts susceptibility to hyperoxia-driven perturbations to lung maturation. Pediatr Pulmonol. 2019;54:1060–77.
21. Will JP, Hirani D, Thielen F, Klein F, Vohlen C, Dinger K, et al. Strain-dependent effects on lung structure, matrix remodeling, and Stat3/Smad2 signaling in C57BL/6N and C57BL/6J mice after neonatal hyperoxia. Am J Physiol Regul Integr Comp Physiol. 2019;317:R169–81.
22. Jiang JS, Chou HC, Chen CM. Cathelicidin attenuates hyperoxia-induced lung injury by inhibiting oxidative stress in newborn rats. Free Radical Bio Med. 2020;150:23–9.
23. Chou HC, Chen CM. Cathelicidin attenuates hyperoxia-induced intestinal injury through inhibition of NF-κB activity in newborn rats. Exp Mol Pathol. 2020;113:104269.
24. Remot A, Descamps D, Noordine ML, Boukadiri A, Mathieu E, Robert V, et al. Bacteria isolated from lung modulate asthma susceptibility in mice. ISME J. 2017;11:1061–74.
25. Huang YJ, Sethi S, Murphy T, Nariya S, Boushey HA, Lynch SV. Airway microbiome dynamics in exacerbations of chronic obstructive pulmonary disease. J Clin Microbiol. 2014;52:2813–23.
26. Mogayzel PJ, Naureckas ET, Robinson KA, Mueller G, Hadjiliadis D, Hoag JB, et al. Cystic fibrosis pulmonary guidelines chronic medications for maintenance of lung health. Am J Resp Crit Care. 2013;187:680–9.

27. Dolma K, Freeman AE, Rezonzew G, Payne GA, Xu X, Jilling T, et al. Effects of hyperoxia on alveolar and pulmonary vascular development in germ-free mice. Am J Physiol Lung Cell Mol Physiol. 2020;318:L421–8.
28. Singh N, Vats A, Sharma A, Arora A, Kumar A. The development of lower respiratory tract microbiome in mice. Microbiome. 2017;5:61.
29. Berg RD, Garlington AW. Translocation of certain indigenous bacteria from the gastrointestinal tract to the mesenteric lymph nodes and other organs in a gnotobiotic mouse model. Infect Immun. 1979;23:403–11.
30. Berg RD. Bacterial translocation from the gastrointestinal tract. Adv Exp Med Biol. 1999;473:11–30.
31. Chou HC, Li YT, Chen CM. Human mesenchymal stem cells attenuate experimental bronchopulmonary dysplasia induced by perinatal inflammation and hyperoxia. Am J Transl Res. 2016;8:342–53.
32. Irwin D, Helm K, Campbell N, Imamura M, Fagan K, Harral J, et al. Neonatal lung side population cells demonstrate endothelial potential and are altered in response to hyperoxia-induced lung simplification. Am J Physiol Lung Cell Mol Physiol. 2007;293:L941–51.
33. Chiu CJ, Scott HJ, Gurd FN. Intestinal mucosal lesion in low-flow states. II. The protective effect of intraluminal glucose as energy substrate. Arch Surg. 1970;101:484–8.
34. Callahan BJ, McMurdie PJ, Rosen MJ, Han AW, Johnson AJ, Holmes SP. DADA2: High-resolution sample inference from Illumina amplicon data. Nat Methods. 2016;13:581–3.
35. Callahan BJ, Sankaran K, Fukuyama JA, McMurdie PJ, Holmes SP. Bioconductor workflow for microbiome data analysis: from raw reads to community analyses. F1000Res. 2016;5:1492.
36. Quast C, Pruesse E, Yilmaz P, Gerken, J, Schweer T, Yarza P, et al. The SILVA ribosomal RNA gene database project: improved data processing and web-based tools. Nucleic Acids Res. 2013;41:D590–6.
37. Schliep KP. phangorn: phylogenetic analysis in R. Bioinformatics. 2011;27:592–3.
38. McMurdie PJ, Holmes S. phyloseq: an R package for reproducible interactive analysis and graphics of microbiome census data. PLoS one. 2013;8:e61217.
39. Segata N, Izard J, Waldron L, Gevers D, Miropolsky L, Garrett WS, et al. Metagenomic biomarker discovery and explanation. Genome Biol. 2011;12:R60.
40. Asnicar F, Weingart G, Tickle TL, Huttenhower C, Segata N. Compact graphical representation of phylogenetic data and metadata with GraPhlAn. PeerJ. 2015;3:e1029.
41. Milan M, Maroso F, Dalla Rovere G, Carraro L, Ferraresso S, Patarnello T, et al. Tracing seafood at high spatial resolution using NGS-generated data and machine learning: Comparing microbiome versus SNPs. Food Chem. 2019;286:413–
42. Pietrucci D, Teofani A, Unida V, Cerroni R, Biocca S, Stefani A, et al. Can gut microbiota be a good predictor for Parkinson's disease? a machine learning approach. Brain Sci. 2020;10:242.

Tables

Table 1 Hyperoxia-induced bacterial translocation from the intestine to the lung

	Intestine		Lung	
Genus	RA	O_2	RA	O_2
CAG-56	1.3E-05±2.2E-05	3.40E-04±7.80E-04	ND	2.30E-04±3.70E-04
Clostridia_Family_XIII_ge	2.0E-05±4.0E-05	5.00E-05±6.00E-05	ND	6.30E-05±1.60E-04
Coriobacteriales_Incertae_Sedis_ge	1.1E-04±7.0E-05	1.70E-04±1.90E-04	ND	1.80E-04±4.60E-04
Enterobacter	1.6E-02±1.9E-02	8.80E-05±1.20E-04	ND	7.40E-04±1.30E-03
Howardella	7.5E-05±7.8E-05	6.80E-05±1.40E-04	ND	1.40E-04±3.50E-04
Muribaculum	4.9E-05±4.4E-05	2.40E-05±6.00E-05	ND	1.70E-04±4.30E-04
Peptococcaceae_ge	5.7E-05±6.7E-05	2.20E-05±4.60E-05	ND	1.60E-04±3.50E-04
Ruminococcaceae_UCG-010	8.6E-05±6.5E-05	2.50E-04±2.70E-04	ND	5.50E-04±8.50E-04
Sellimonas	4.6E-05±8.7E-05	1.20E-04±2.30E-04	ND	3.80E-05±1.30E-04
Weissella	2.0E-05±3.7E-05	3.30E-05±4.80E-05	ND	2.00E-04±5.10E-04

ND, non-detectable.

Table 2 Correlation between the relative abundance of bacterial taxa that lung microbiota translocated from intestine and pulmonary inflammatory cytokines

		IL-1β	TNF-α	MIP-2	CAG-56	Clostridia_Family_XIII_ge	Clostridium_sensu_stricto_1	Coriobacteriales_Incertae_Sedis	Enterobacter	Howardella	Muribaculum	Peptococcaceae	Ruminococcaceae_UCG-010	Sellimonas	Weissella
Spearman's rho	IL-1β	1													
	TNF-α	0.21	1												
	MIP-2	**0.567***	0.038	1											
	CAG-56	0.326	**0.656****	0.101	1										
	Clostridia_Family_XIII_ge	0.183	**0.542***	0.013	**0.651****	1									
	Clostridium_sensu_stricto_1	-0.095	-0.191	-0.172	-0.244	-0.31	1								
	Coriobacteriales_Incertae_Sedis_ge	0.202	0.299	0.178	**0.646****	-0.125	-0.128	1							
	Enterobacter	0.339	-0.097	0.402	0.131	-0.157	0.342	0.239	1						
	Howardella	0.21	0.21	0.397	-0.128	-0.086	-0.023	-0.086	-0.108	1					
	Muribaculum	**0.475***	-0.07	0.406	-0.187	-0.125	-0.127	-0.125	0.396	-0.086	1				
	Peptococcaceae_ge	**0.494***	0.24	0.214	0.39	0.239	-0.316	0.34	0.291	-0.108	0.396	1			
	Ruminococcaceae_UCG-010	0.413	**0.594****	-0.065	**0.748****	**0.602****	0.061	0.276	0.131	-0.128	-0.187	0.096	1		
	Sellimonas	**0.546***	0.289	0.083	0.282	0.434	-0.27	-0.125	-0.157	-0.086	0.375	0.285	0.282	1	
	Weissella	0.398	0.397	-0.164	**0.481***	**0.642****	-0.164	-0.086	-0.108	-0.059	-0.086	0.468	**0.481***	**0.728****	1

*P < 0.05, **P < 0.01.

Table 3 Predictive performance using genus-level intestinal and lung microbiota on different machine learning algorithms for predicting RA- or hyperoxia-reared mice.

Machine learning	Accuracy	Sensitivity	Specificity	AUC
Bayes network	0.944	0.889	1.000	0.963
Decision tree	0.889	0.889	0.889	0.840
k-nearest neighbor	0.778	0.556	0.556	0.778

AUC, area under the curve.

Figures

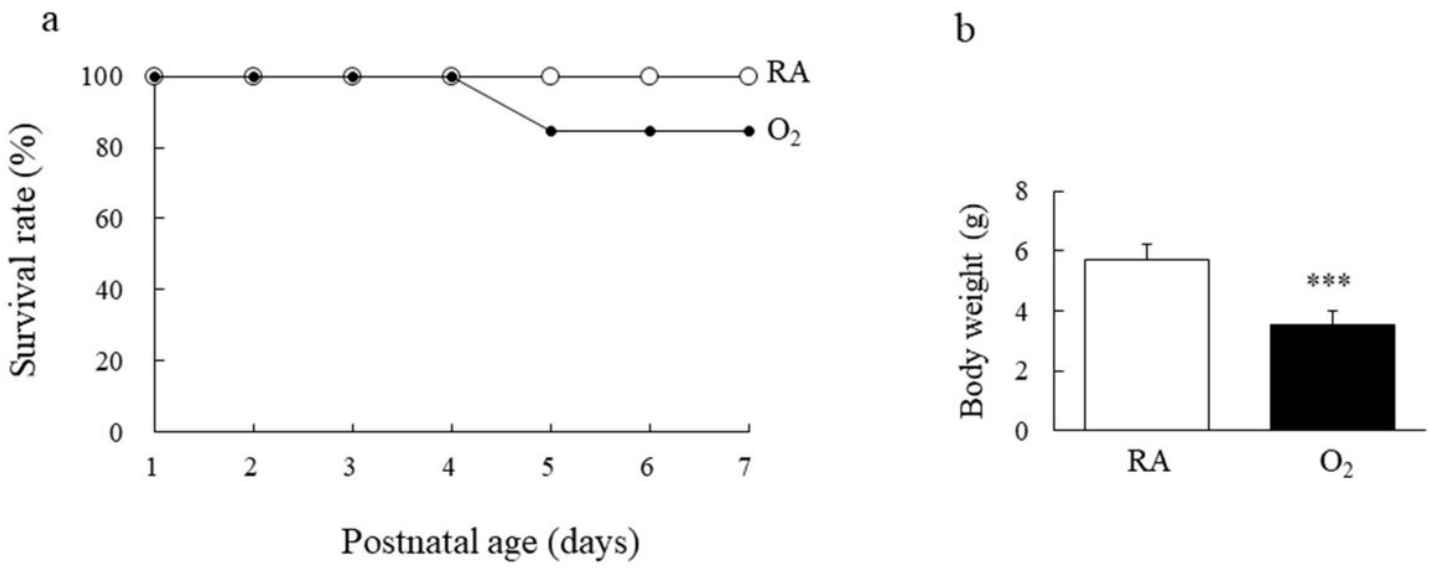

Figure 1

Effects of hyperoxia on (a) survival rate and (b) body weight on postnatal day 7. All nine mice reared in RA survived. However, two mice reared in O2-enriched air died on postnatal day 5. Mice reared in hyperoxia exhibited a significantly lower body weight on postnatal day 7 than did those reared in RA. Data are presented as mean ± SD. ***P < 0.001. RA, room air.

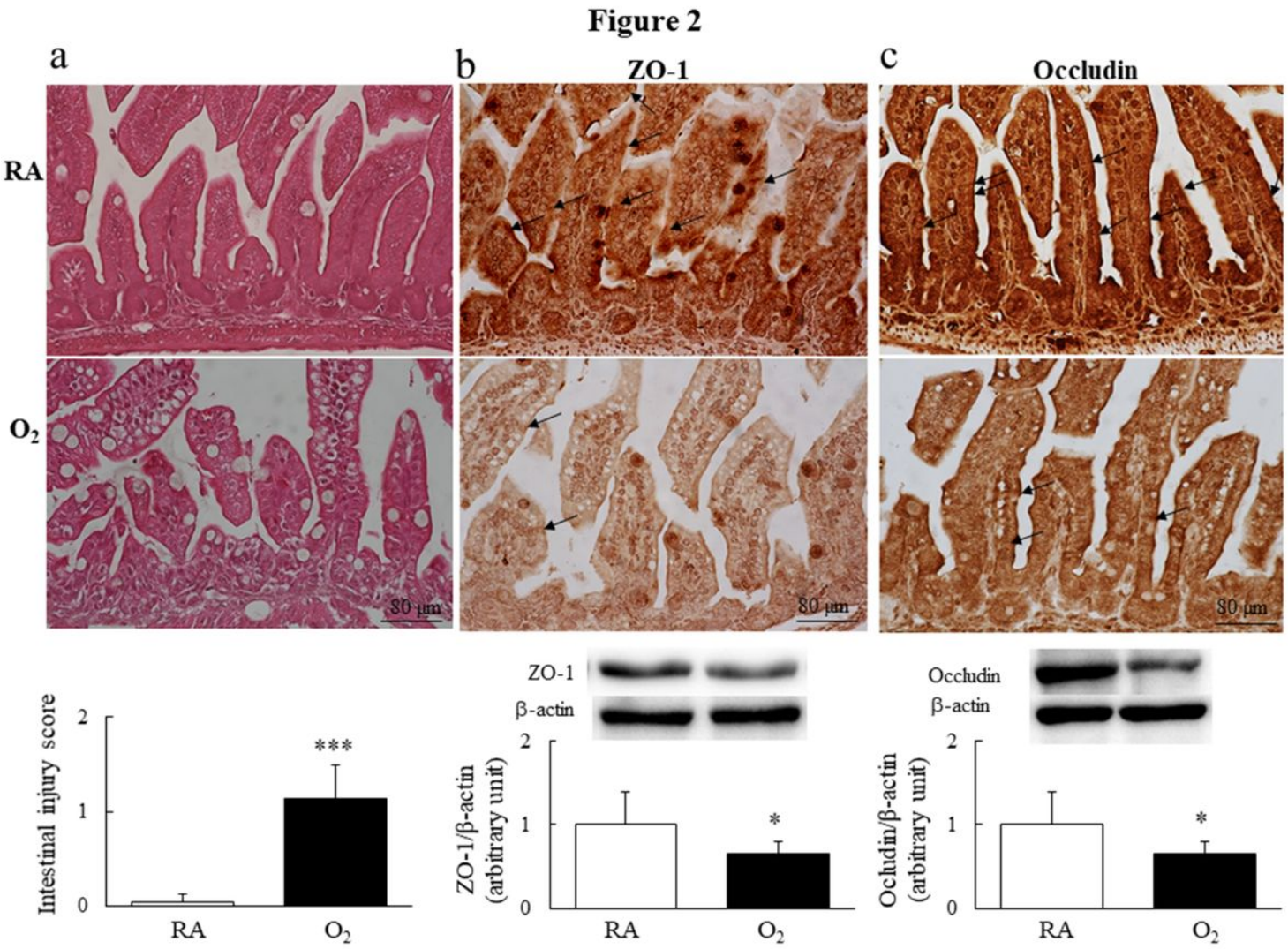

Figure 2

Hyperoxia-induced intestinal injury and decreased intestinal tight junction expression on postnatal day 7. (a) Representative intestinal sections from mice exposed to postnatal RA or hyperoxia that were stained with hematoxylin and eosin. The mice reared in RA exhibited a normal intestinal mucosal framework, and the mice reared in hyperoxia had malalignment and distended basolateral intercellular spaces in the epithelium; additionally, they exhibited a significantly higher intestinal injury score than did RA-reared mice. (b) Representative immunohistochemistry and (c) Western blotting for occludin and ZO-1. Both occludin and ZO-1 (arrow) were observed on the side adjacent to the cell membranes of the enterocytes. The hyperoxia-reared mice exhibited disrupted occludin and ZO-1 immunohistochemistry between adjacent enterocytes. The hyperoxia-reared mice exhibited significantly lower occludin and ZO-1 protein levels than did RA-reared mice. Data are presented as mean ± SD. *P < 0.05, ***P < 0.001. RA, room air.

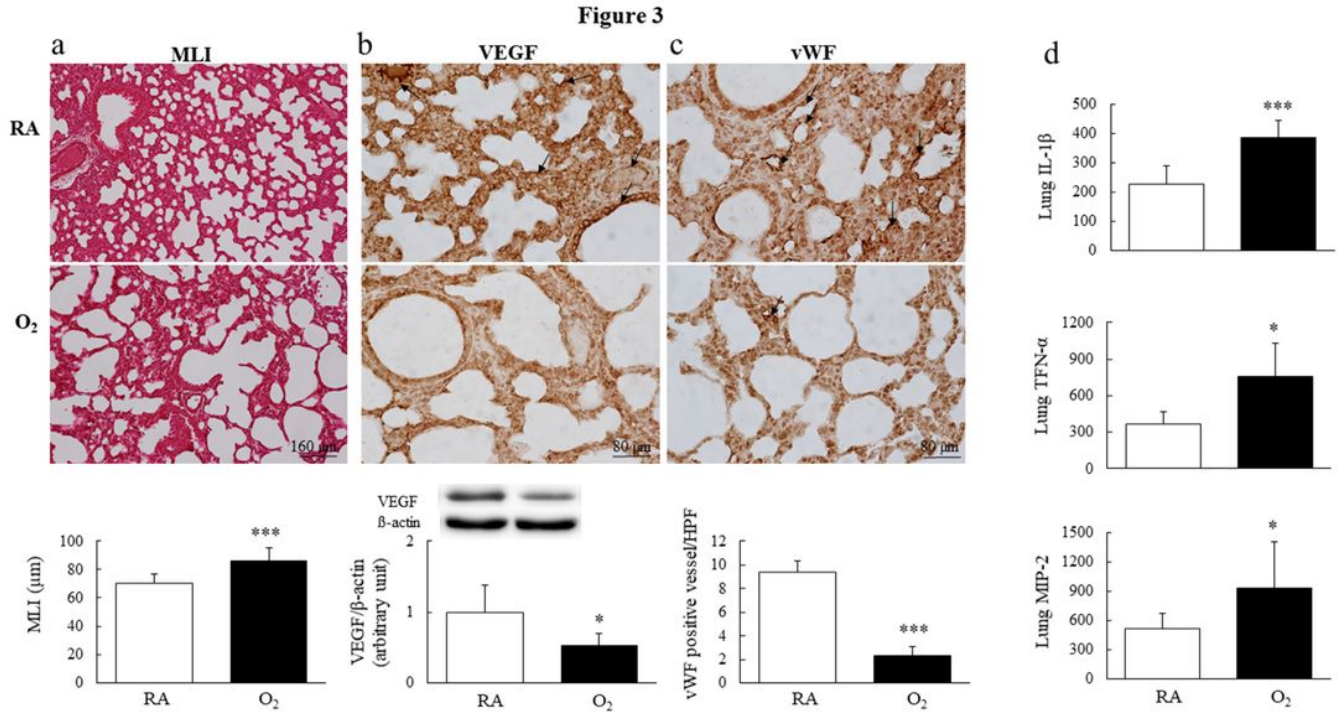

Figure 3

Hyperoxia-impaired alveolarization and angiogenesis and increased lung cytokines on postnatal day 7. (a) Representative lung sections from mice exposed to postnatal RA or hyperoxia that were stained with hematoxylin and eosin. Those from mice reared in hyperoxia exhibited large thin-walled air spaces and significantly higher MLI values than did those from mice reared in RA. (b) Representative immunohistochemistry, (c) Western blotting for VEGF and vWF, and (d) lung cytokines. The mice reared in hyperoxia exhibited decreased VEGF (arrow) and vWF (arrow) immunoreactivity. Western blot analysis and semiquantitative analysis revealed that the mice reared in hyperoxia exhibited significantly decreased VEGF protein expression and vascular density than did those reared in RA. The mice reared in hyperoxia exhibited significantly higher IL-1β, TNF-α, and MIP-2 levels than did those reared in RA. Data are presented as mean ± SD. *P < 0.05, ***P < 0.001. RA, room air.

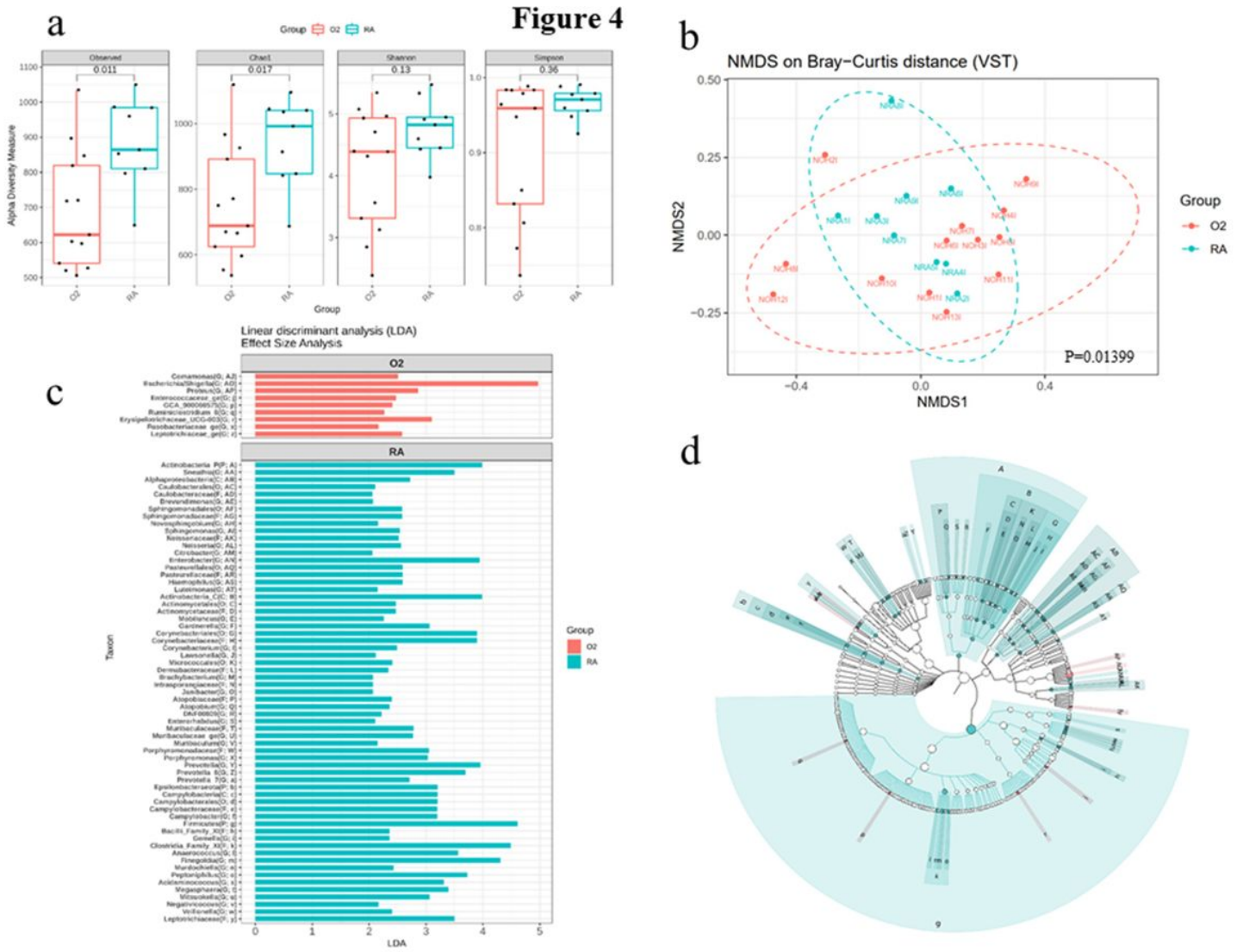

Figure 4

Dysbiosis of gut microbiota patterns in the hyperoxia-reared and RA-reared mice on postnatal day 7. (a) Comparison of alpha diversity indices (observed, Chao1 index, Shannon, and Simpson) between the hyperoxia-reared and RA-reared mice. (b) NMDS plots based on Bray–Curtis distances showed significant differences between the hyperoxia-reared and RA-reared mice. (c) LDA effect size identified the most differentially abundant taxa between the hyperoxia-reared and RA-reared mice. Significant biomarkers were defined as taxa with LDA scores (log10) ≥ 2. (d) Significant taxa are highlighted on the cladogram. P: Phylum; C: Class; O: Order; F: Family; G: Genus.

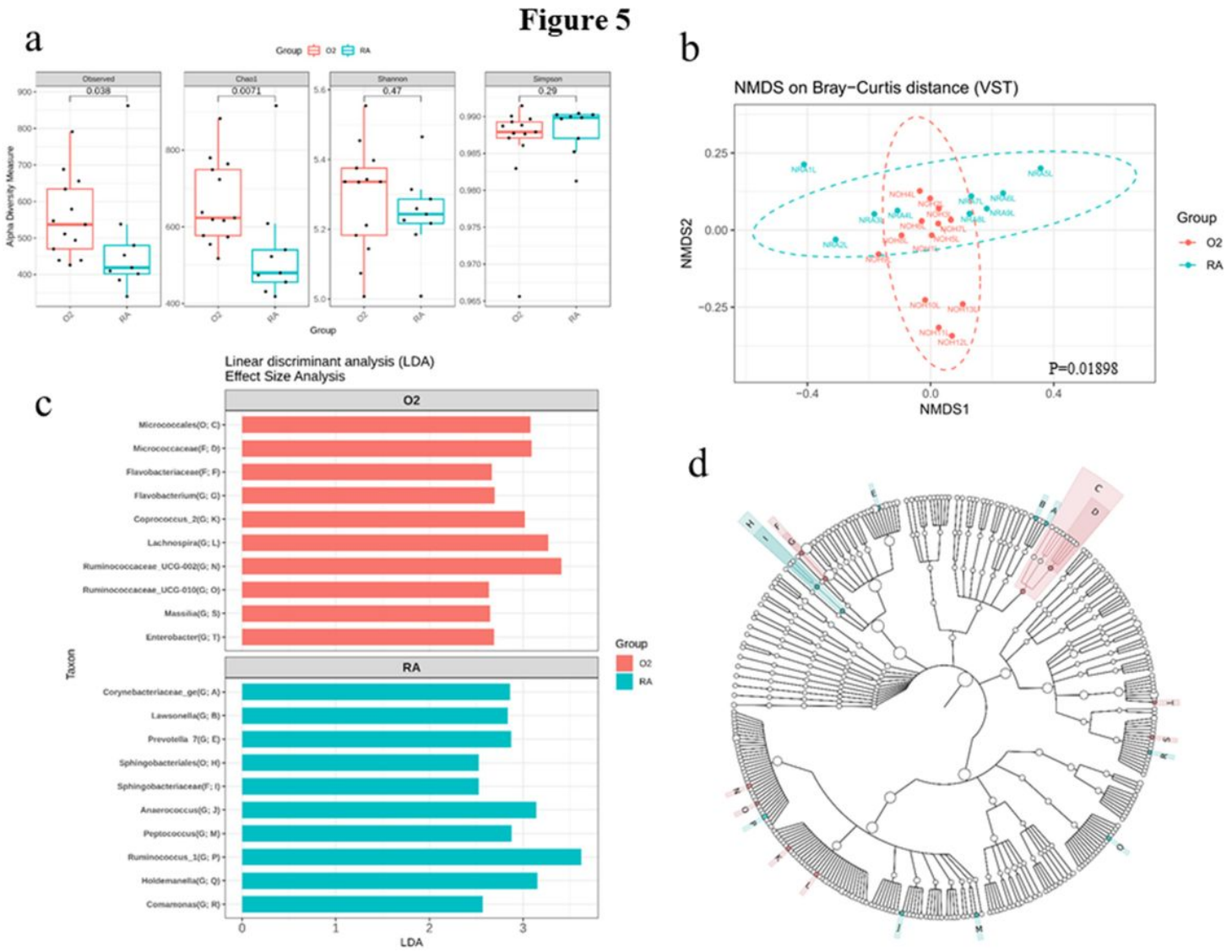

Figure 5

Dysbiosis of lung microbiota patterns in the hyperoxia-reared and RA-reared mice on postnatal day 7. (a) Comparison of alpha diversity indices (observed, Chao1 index, Shannon, and Simpson) between the hyperoxia-reared and RA-reared mice. (b) NMDS plots based on Bray–Curtis distances showed significant differences between the hyperoxia-reared and RA-reared mice. (c) LDA effect size identified the most differentially abundant taxa between the hyperoxia-reared and RA-reared mice. Significant biomarkers were defined as taxa with an LDA score (log10) ≥ 2. (d) Significant taxa are highlighted on the cladogram. P: Phylum; C: Class; O: Order; F: Family; G: Genus.

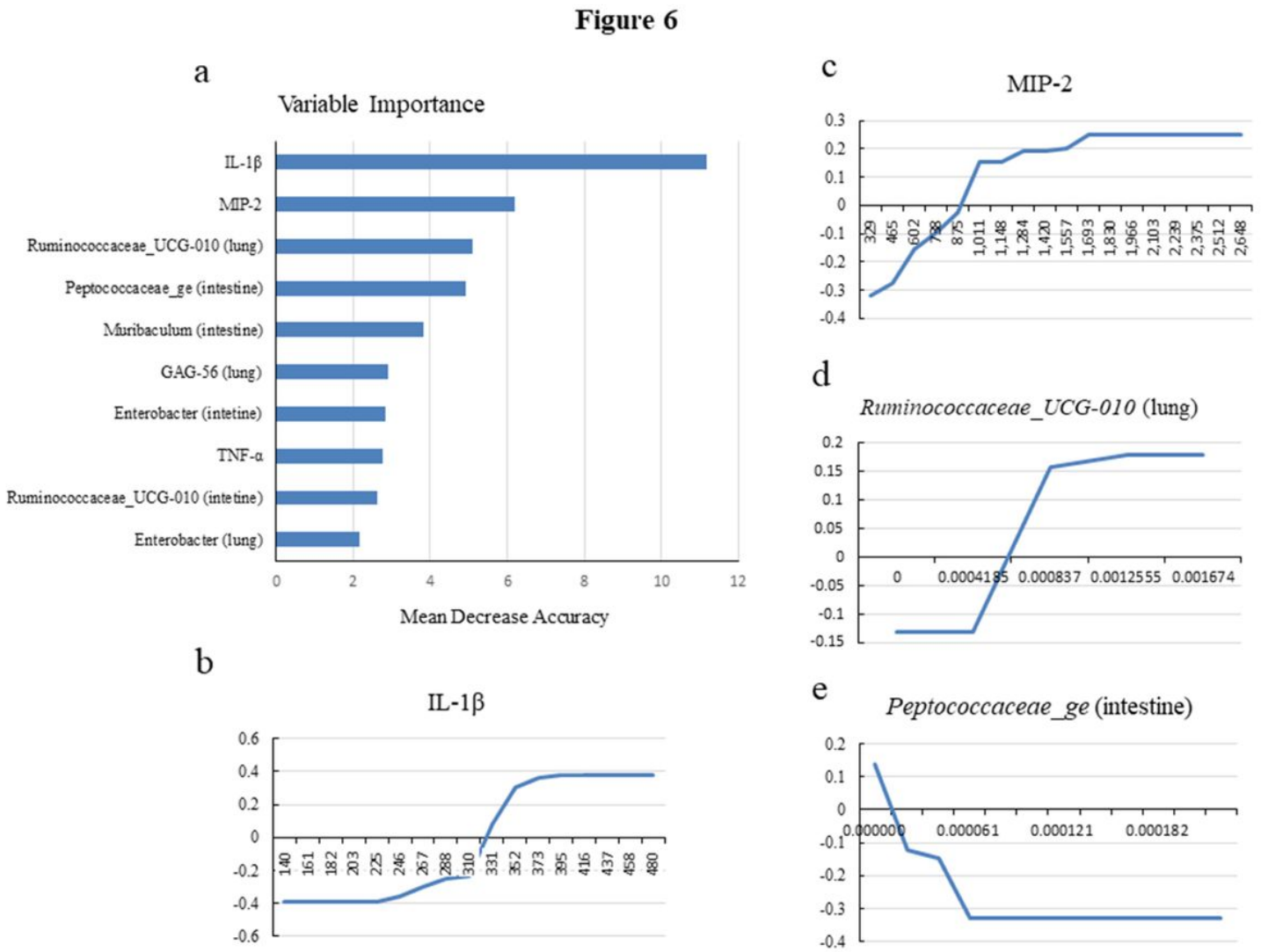

Figure 6

Rankings of important variables and partial dependence plots for the most influential cytokines and microbiota. (a) Ranking of important variables according to the mean decrease in accuracy in the random forest machine learning algorithm. To further depict the effects of important variables affecting hyperoxia, partial dependence plots on the most influential cytokines and microbiota were analyzed for (b) IL-1β, (c) MIP-2, (d) Ruminococcaceae_UCG-010 (lung), and (e) Peptococcaceae_ge (intestine).